Progress In Electromagnetics Research C, Vol. 133, 65–79, 2023

Deep Learning Assisted Distorted Born Iterative Method for Solving Electromagnetic Inverse Scattering Problems

Harisha Shimoga Beerappa*, Mallikarjun Erramshetty, and Amit Magdum

Abstract—This paper presents the deep learning-assisted Distorted Born Iterative Method (DBIM) for the permittivity reconstruction of dielectric objects. The inefficiency of DBIM to reconstruct strong scatterers can be overcome if it is supported by Convolutional Neural Network (CNN). A novel approach, cascaded CNN is used to obtain a fine-resolution estimate of the permittivity distribution. The CNN is trained using images consisting of MNIST digits, letters, and circular objects. The proposed model is tested on synthetic data with different signal-to-noise ratios (SNRs) and various contrast profiles. Thereafter, it is verified through experimental data provided by the Institute of Fresnel, France. Reconstruction results show that the proposed inversion method outperforms the conventional DBIM method in terms of accuracy and convergence rate.

1. INTRODUCTION

Microwave imaging is a noninvasive, and non-contact technology to evaluate hidden or embedded objects in a structure using electromagnetic waves in the microwave regime. Electromagnetic Inverse Scattering Problems (EISPs) are widely used in nondestructive testing, geophysical explorations, biomedical imaging and diagnosis, through-wall imaging, remote sensing, security checks, and other domains [1, 2]. Many nonlinear imaging techniques are developed over the years to obtain an efficient reconstruction. Among them, contrast source inversion (CSI) [3], distorted Born iterative method (DBIM) [4], and subspace-based optimization (SOM) [5] are the most recently developed and popular nonlinear iterative methods. The main drawback of these methods is that as the nonlinearity of the problem increases, the solution converges to a local minimum. Also, the convergence time for these methods is high. Therefore, these methods are not suitable for real-time applications. In this framework, deep learning-based methods play a vital role for quantitative imaging purposes. Deep learning has become one of the most powerful methods in the field of regression and classification issues in recent years. These methods are much faster and produces better image quality than the conventional iterative methods based on optimization [6]. Deep learning algorithms are currently being employed in microwave imaging techniques to produce an inverse solution in real time because of its effective nonlinear matching capability and one-step testing procedure.

In the literature, there are very few works devoted to the application of convolutional neural network (CNN) to address EISPs [6–12]. CNN is used for post-processing the initial reconstruction by the Backpropagation algorithm [8, 9]. Discretized filtered back projection (FBP) applied to the scatter field is used for CNN in [6]. Direct inversion from the scattered field is tested in [8]. In [10], deep learning is applied in two steps, and [9] proposes a multi-layer complex-valued residual CNN cascade to process an initial guess obtained by Backpropagation algorithm. The output of CNN is iteratively refined in [11]. The Subspace-Based Variational Born Iterative Method (SVBIM) is used to generate the initial guess, and U-Net-based Deep Learning (DL) approach is used to solve quantitative inverse

Received 7 April 2023, Accepted 15 May 2023, Scheduled 24 May 2023
* Corresponding author: Harisha Shimoga Beerappa (harishasb@jnnce.ac.in).
The authors are with the Electronics and Communication Engineering Department, National Institute of Technology Goa, India.

problem [12]. Neural network methods are applied to solve inverse problems [13–15]. The applicability of deep-learning for the reconstruction of DBIMs has not been explored as per authors' best of knowledge, hence we proposed this work along with novel cascaded CNN approach. In this work, an initial guess obtained by the DBIM is fed to CNN1, and the obtained image is further improved by cascading CNN2. This improved initial guess from CNN2 is given to iterative DBIM to get final results. It is worth mentioning that the performance of DBIM with deep learning has not been stated before.

U-Net is one of the encoder-decoder CNN architecture with skip connections, used exclusively for image segmentation [16]. Instead of learning an entirely new mapping function from the low-resolution to the high-resolution image, the U-Net learns to anticipate the missing high frequency components from low-resolution image. Therefore, this architecture is commonly employed to solve EISPs. A U-Net architecture having an encoder depth of 3 (Totally 45 layers) is used in the proposed model.

The mapping of the scattered fields directly to ground truth or any initial guess to ground truth through a single CNN has less efficiency; hence, the proposed model consists of a cascade of two CNNs followed by iterative refinement using DBIM for five iterations, which improves the reconstruction quantitatively and qualitatively. The proposed model is trained using MNIST digits, letters, and circular objects. Various examples of synthetic and experimental data sets [17] are used to validate the proposed model's performance. The results are excellent in terms of convergence rate and reconstruction quality.

This paper is organized as follows. The problem formulation is covered in Section 2. DBIM algorithm is briefed in Subsection 2.1, and CNN for Inverse Problems is discussed in Section 2.2. The proposed reconstruction algorithm is described in Section 3. Thereafter, numerical results are reported in Section 4. Finally, Section 5 contains the concluding remarks.

2. PROBLEM FORMULATION

A two-dimensional (2-D) transverse magnetic (TM) situation is considered. The circular configuration [18] considered in this paper is as shown in Figure 1. The investigation domain Ω contains the object of interest, which has permittivity variation in the x-y plane. This object is in a media with a homogeneous background. TM waves created by the N_{tx} number of transmitting antennas illuminate the unknown scatterers, and the scattered field is measured by the N_{rx} number of receiving antennas for each incidence. The measuring domain circle denoted by Γ is uniformly distributed with transmitters T_x and receivers R_x.

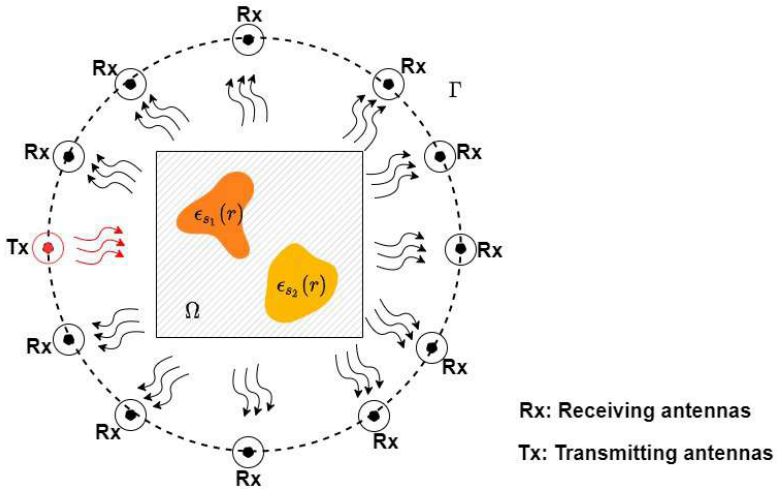

Figure 1. Configuration of a microwave imaging system for two-dimensional inverse scattering.

The integral equations for the relationship between scattered fields and the contrast function are as follows [1]:

$$u(\underline{r}) = u^{inc}(\underline{r}) + j\omega\mu_b \int \chi(\underline{r}')u(\underline{r}')G(r,\underline{r}')d\underline{r}', \quad \underline{r}, \underline{r}' \in \Omega \tag{1}$$

$$u^{scat}(\underline{r}) = j\omega\mu_b \int \chi(\underline{r'})u(\underline{r'})G(r,\underline{r'})d\underline{r'}, \quad \underline{r} \in \Gamma, \underline{r'} \in \Omega \tag{2}$$

The incident field, scattered field, and total field are denoted by u^{inc}, u^{scat}, and u, respectively. $\underline{r}, \underline{r'} \in (x, y)$ are spatial variables that indicate the Cartesian coordinates of the receivers and emitter, respectively. μ_b denotes the magnetic permeability, and ω is the working frequency. The symbol j denotes the imaginary number such that $j^2 = -1$, and the free-space Green's function is denoted by $G(\underline{r}, \underline{r'})$. The test domain and observation domain are indicated by Ω and Γ, respectively. The contrast function χ expresses the difference between the homogeneous background and the scatterer. It is written as $\chi = (\epsilon_r/\epsilon_b - 1)$, where ϵ_r and ϵ_b are the target's and background's relative permittivity, respectively.

The solution to Equations (1) and (2) can be found by applying method of moments to transform them into discrete matrix equations [19, 20]. The matrices that result are

$$\mathbf{u} = \mathbf{u}^{inc} + [G^d][u]\boldsymbol{\chi} \tag{3}$$

$$\mathbf{u}^{scat} = [G^s][u]\boldsymbol{\chi} \tag{4}$$

where $[G^d]$ represents an internal radiation operator, while $[G^s]$ represents an external radiation operator. [ ] implies that the variable is a matrix, while the bold letters imply that it is a vector. In an inverse scattering problem, the terms $[G^s]$, $\mathbf{u}^{inc}$, and $\mathbf{u}^{scat}$ are known, whereas $\boldsymbol{\chi}$ and $[u]$ are unknown. This problem can be solved using the nonlinear model of DBIM.

2.1. DBIM Assisted Deep Learning Scheme

DBIM was proposed by Chew and Wang [4], for solving the nonlinear minimization problem through an iterative procedure. This algorithm alternately updates the contrast estimates and the total field within the imaging domain. In DBIM, the cost function is chosen as the quadratic error of mismatch of measured scattered field and the predicted one. In addition, a Tikhonov regularization term is added to the cost function to stabilize the optimization procedure. The cost function is defined as [24]

$$\delta_{\chi_n} = \arg\min_{\delta_\chi} \left(\sum_{k=1}^{K} \left\| u_k^{scat} - G^s \chi u_k^b - G^{bs} \delta_\chi u_k^b \right\|_2^2 + \lambda \left\| \delta_\chi \right\|_2^2 \right) \tag{5}$$

where u_k^b denotes the secondary incident field in the presence of inhomogeneous background medium, G^{bs} an inhomogeneous background Green's function, λ the Tikhonov regularization parameter, and $K\,(k = 1, 2, ..., K)$ the number of incident fields. The DBIM needs to compute $G^{bs,n}$ and $u_{k,n}^b$ for each iteration as

$$G^{bs,n} = G^s \left(I - \chi_n G^d \right)^{-1} \tag{6}$$

$$u_{k,n}^b = \left(I - G^d \chi_n \right)^{-1} u_k^{inc} \tag{7}$$

By minimizing the cost function, the following matrix equation is obtained

$$\left(A^\dagger A + \lambda I \right) \delta_{\chi_n} = A^\dagger \delta u_{k,n}^{scat} \tag{8}$$

where $A = G^{bs,n} u_{k,n}^b$ and $\delta u_{k,n}^{scat} = u_k^{scat} - G^s \chi_n u_{k,n}^{scat}$. Once δ_n is estimated, the solution is updated as

$$\chi_{n+1} = \chi_n + \delta_{\chi_n} \tag{9}$$

Finally, the residual error value is calculated. If a certain stopping criterion is satisfied, the iterative process terminates. Otherwise, it continues.

Traditional iterative strategies typically initialize the search for contrast function χ from the origin. Hence, the chances of falling into local minima on the way to global minima are greater [11]. Motivated by the DeepInverse network [9] and CS-Net [11], an iterative solution for nonlinear electromagnetic inverse scattering is obtained through deep learning. In the proposed method, the DBIM first iteration estimate is used as an initial guess. As a result, the problem of local minima is no longer an issue over a wider range of object permittivities. CNN uses a rough estimate of the contrast function as input and produces a fine estimate of the contrast function. During CNN training, it learns an underlying prior about objects having similar contrast.

2.2. CNN for Inverse Problems

The proposed deep learning method for solving inverse scattering problems is implemented using U-Net architecture [16] with an encoder-decoder depth of 3 as shown in Figure 2. Since the U-Net architecture was originally designed for segmentation, it is modified such that the Softmax layer is removed, and the segmentation layer is replaced with a regression layer. The recent works published in this area [8, 12, 25, 26] show that the U-Net is well suited for solving Inverse Scattering Problem (ISP) along with back-propagation, contrast source inversion, SVBIM, etc. U-Net architecture consists of convolutional and downsampling layers (contraction path), followed by successive upsampling and convolutional layers (expansion path). A collection of convolutional layers and rectified linear units (ReLU) comprise the contracting path, which is followed by a max-pooling operation. The purpose of this path is to capture the context of the input image. The expansive path is identical to a contracting path, but the max-pooling in the contracting path is replaced by an up convolution. Additionally, in the expansive path, there are three concatenations with the corresponding feature maps from the contracting path. The purpose of this path is to combine precise localization with contextual information from the contracting path. The bridge is then used to connect the contracting and expanding paths. It is built using two convolutional layers and a dropout layer. Concatenation of corresponding blocks is indicated by the blocks with two colours in the expansive path [16]. The spatial information diminishes throughout the contraction path, whereas the feature information grows during the expansion path. Within the U-Net architecture, the features and spatial information are concatenated using a 3×3 up-convolution. It assures that the input and output in the training have a one-to-one correspondence, and the trained U-Net can perform quantitative microwave imaging. Since the U-Net architecture was originally designed for segmentation, the Softmax layer is removed, and the segmentation layer is replaced with a regression layer. Skip connections provide the details needed to reconstruct accurate shapes for segmentation boundaries. The addition of skip connections recovers the fine-resolution details. The skip connections enhance the optimization process by preventing gradients from vanishing [16].

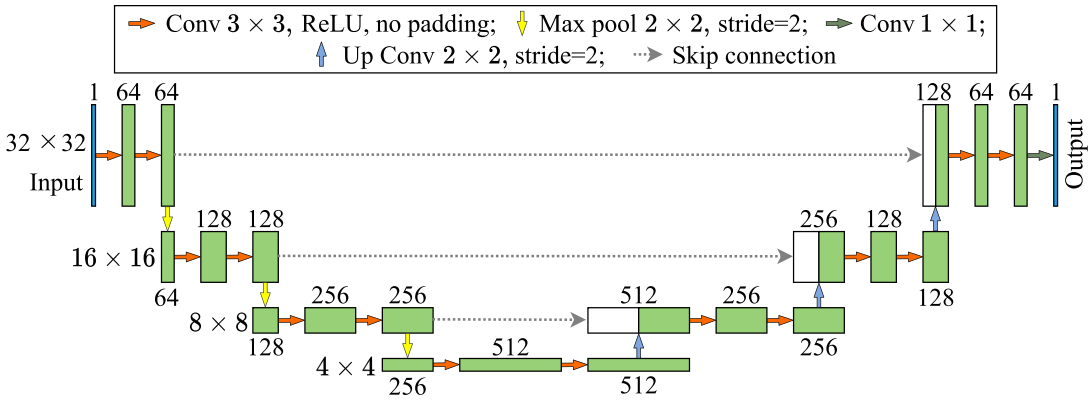

Figure 2. Architecture details of U-Net for the proposed model.

In this paper, the true contrast is employed as the network's target, while the initial contrast function derived by solving DBIM at the first iteration is used as the input to the U-Net. During the contraction process, spatial information decreases while feature information increases. The characteristics and spatial information are concatenated in the U-Net architecture using a three-dimensional up-convolution. It guarantees that the training input and output are consistent and that the trained U-Net can perform quantitative microwave imaging.

The use of additional CNN modules will enable the incorporation of more multiple scattering effects into account [9] or decreases the nonlinearity of the objective function [27], leading to an improved image equality. The optimum batch size recommended in [28] is 32 or 64 with smaller learning rate. Empirically we have set the batch size of 32 with learning rate of 0.0003. as CNN1 is trained using 4800 images, it needs 150 iterations (batch size $\times$ no. of iterations = total no. of training data). Similarly, CNN2 is trained for 300 iterations, as the training data is 9600. The effect of overfitting is mitigated

by empirically stopping the training of CNN1 and CNN2 at the 30th and 50th epochs, respectively.

3. PROPOSED INVERSION METHOD

Deep neural networks are naturally well-suited for nonlinear EM inverse scattering problems [9]. The mapping of the scattered field directly to ground truth or any initial guess to ground truth through a single CNN has less efficiency [8], hence a novel cascaded CNN using U-Net architecture and DBIM algorithm is proposed to gradually map scattered fields to ground truth. The proposed scheme for embedding deep learning in DBIM as shown in Figure 3 takes the DBIM first iteration estimation as input and outputs the fine-resolution estimate of the permittivity distribution. The CNN learns the relationship between input and output by updating the network's weight matrix and bias. Initially, the first iterative solution is obtained using the DBIM, which makes use of the measured scattered field and the zero initial guess. Next, this estimated solution is fed to the cascaded CNNs (CNN1 and CNN2). CNN2 takes CNN1's output as input and maps it to ground truth. While iteratively refining the CNN2 output, the DBIM saturates before the fifth iteration. Hence, the output of CNN2 is iteratively refined using DBIM (with five iterations), which helps to reconstruct the shape and enhances the accuracy, and thus improves the reconstruction quantitatively and visibly. The training of CNN1 and CNN2 is shown in Figures 4 and 5, respectively. CNN1 is trained using 4800 profiles, whereas CNN2 is trained using 9600 profiles.

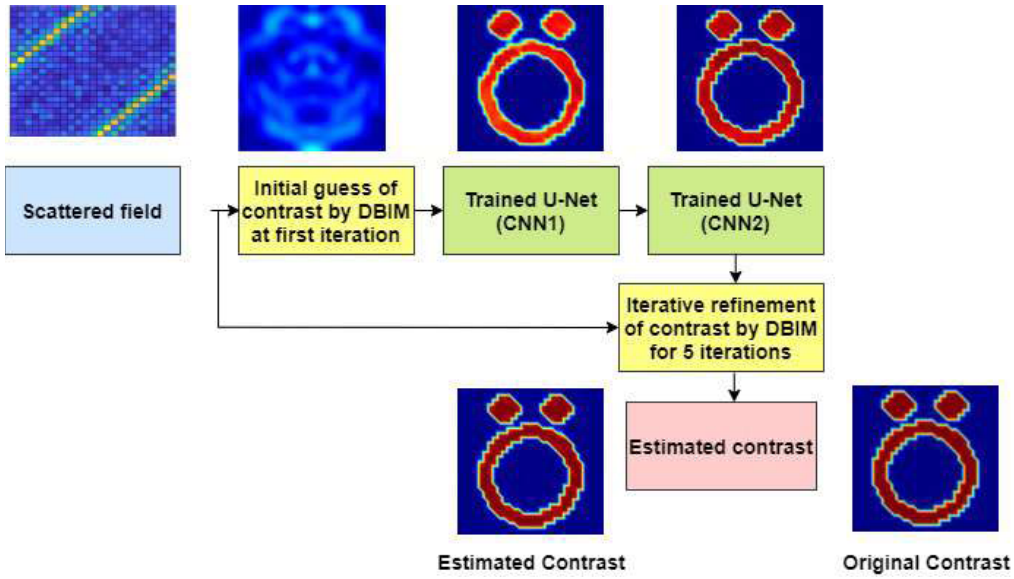

Figure 3. Proposed scheme for embedding deep learning in DBIM with images at each stage.

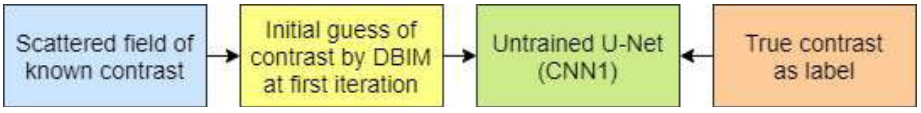

Figure 4. Training CNN1 using DBIM first iteration estimate.

The following steps are involved in training and testing the proposed scheme.

(i) CNN1 is trained using 4800 images consisting of MNIST digits (3500), letters (500), and circular objects (800). The MNIST [21] dataset images of size 28×28 are used to generate the dielectric objects of size 32×32. The permittivity of the objects is set between 1.2 and 2.5, with the background permittivity of 1. Similarly, CNN2 is trained using 9600 objects consisting of 4800 profiles as described above, and their estimates are obtained by CNN1.

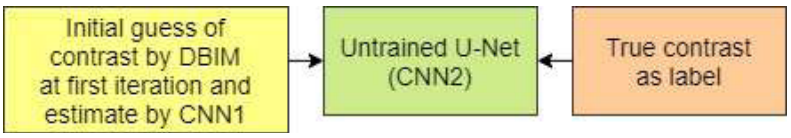

Figure 5. Training CNN2 using estimates obtained by DBIM first iteration and CNN1.

(ii) These dielectric objects are then used to generate the corresponding scattered fields. Here, 24 transceivers are used, which are located uniformly on a circular measurement domain of 0.75 m radius. The operating frequency is 3 GHz. The scattered field is corrupted by the random noise of 5 dB.

(iii) In the inversion algorithm (DBIM), these scattered fields are used as input, which can generate the permittivity distribution over the given investigation domain. This first iteration reconstructed profile is used as input to the CNN.

(iv) The U-Net CNN architecture with an encode-decoder depth of 3 (45 layers) is trained using an initial guess of the contrast profile (absolute value) as input, and the actual contrast profile of step 1 is used as a label. The network is trained with the mean square error (MSE) as a loss function, and the parameters are tuned using the Adam optimizer with a learning rate of 0.0003. CNN1 is trained for 30 epochs with 150 iterations per epoch and a batch size of 32. CNN2 is trained for 50 epochs with 300 iterations per epoch and a batch size of 32.

(v) Trained CNN is tested using 1400 profiles (MNIST dataset, Latin letters, Austria profile, and Fresnel 2005 experimental dataset). The MSE and structural similarity index (SSIM) are used to measure the performance of the proposed model.

3.1. Comparison with Related Method

In [29], deep learning based inversion algorithm is developed to solve the inverse scattering problem using generative adversarial network (GAN). The proposed model and the model proposed by [29] differ as: Firstly, the proposed model consists of Unet CNN whereas [29] used GAN. GAN consists of two neural networks contesting with each other in a game. Given a training set, this technique learns to generate new data with the same statistics as the training set. As GANs are composed of two networks, and each of them has its loss function, results in the fact that GANs are inherently unstable. Secondly, the input to the U-Net is derived from the first iteration of DBIM while [29] used the roughly reconstructed result from a non-iterative method called the Distorted-Born backpropagation scheme. Thus the proposed model is different from [29]. Thirdly, the proposed model is trained using MNIST digits, letters, and circular objects, where as in [29] only MNIST digits are used for training. Therefore, our model has learnt the relationship better.

A related Deep Learning scheme, Subspace-Based Variational Born Iterative Method (SVBIM-DL) is proposed in [12] to solve ISP. Input to the CNN is different in the proposed method compared to that in [12]. U-Net architecture with an encoder depth of 4 is used in [12]. We have used U-Net architecture with an encoder depth of 3. We compare these two approaches quantitatively in Section 4.4.

3.2. Computational Complexity

Let Domain of Investigation (DOI) be discretised into $M \times M$ pixels and N_{DBIM} be the number of iteration in DBIM, then the computational complexity of DBIM is [31, 32]

$$O\left(N_{\mathrm{DBIM}} N_{rx} N_{tx} M^2 \log M^2\right) \tag{10}$$

The key to solve ISPs with low computational complexities is to reduce the value of N_{DBIM} since the values of other parameters in Equation (10) can be barely reduced [8]. The basic operations in CNN are convolutions, ReLU, and pooling. Among them, convolutions dominate the complexity, with the other layers accounting for only 5–10% of the total computing time. The training time is typically three times of that of the testing time for each profile [33].

The total time complexity of all convolutional layers is [33]

$$O\left(\sum_{i=1}^{d} n_{l-1} \cdot s_l^2 \cdot n_l \cdot m_l^2\right) \tag{11}$$

Here l is the index of a convolutional layer, and d is the depth (number of convolutional layers). n_l is the number of filters (also known as "width") in the l^{th} layer. n_{l-1} is also known as the number of input channels of the l^{th} layer. s_l is the spatial size (length) of the filter. m_l is the spatial size of the output feature map [33].

16 convolution layers are present in each CNN module in the proposed system ($d = 16$). Total computational complexity of the proposed model is

$$O\left(2 \cdot \sum_{i=1}^{d} n_{l-1} \cdot s_l^2 \cdot n_l \cdot m_l^2\right) + O\left(6N_{rx}N_{tx}M^2 \log M^2\right) \tag{12}$$

For initial guess, the first iteration of DBIM is used, and finally for reconstructing the value and shape of scatterer, five iterations of DBIM are used. So, totally DBIM is used for only six iterations. The two CNN modules are used in the proposed model. Hence, the proposed model reduces the complexity.

4. RESULTS AND DISCUSSION

The imaging setup consists of a square investigation domain of side 20 cm × 20 cm. Relative permittivities are reconstructed using the noisy scattered field. Lossless dielectrics with nonnegative relative permittivities up to 2.5 are considered as scatterers. MATLAB's Deep Learning toolbox is used to build the U-Net architecture. The proposed scheme is tested for various test images. To estimate image quality, the SSIM and MSE [22] as defined in Equations (13) and (14) are used as qualitative assessment metrics.

$$\text{MSE} = \frac{\sqrt{\sum_{i=1}^{N} (\chi_{oi} - \chi_{ri})^2}}{\sqrt{\sum_{i=1}^{N} (\chi_{oi})^2}} \tag{13}$$

where χ_o is the contrast function of original profile, χ_r the contrast function of the reconstructed profile, and N the total number of values in contrast function. The SSIM [23] index between χ_o and χ_r is

$$\text{SSIM}(\chi_o, \chi_r) = \frac{(2\mu_{\chi_o}\mu_{\chi_r} + C_1)(2\sigma_{\chi_o\chi_r} + C_2)}{(\mu_{\chi_o}^2 + \mu_{\chi_r}^2 + C_1)(\sigma_{\chi_o}^2 + \sigma_{\chi_r}^2 + C_2)} \tag{14}$$

where μ_{χ_o} and μ_{χ_r} are local means; σ_{χ_o} and σ_{χ_r} are standard deviations; $\sigma_{\chi_o\chi_r}$ is the cross covariance of signals χ_o and χ_r. Regularization constants C_1 and C_2 are used to prevent instability in locations where the local mean or standard deviation is near zero. As a result, for such constants, minimal non-zero values should be chosen.

4.1. Tests with Homogeneous Scatterers

The proposed scheme is tested for the MNIST dataset, and the reconstruction results for some representative examples are shown in Figure 6. The results reveal that the suggested method outperforms the DBIM algorithm in reconstructing high-quality images. The SSIM and MSE for these examples are presented in Table 1. It indicates that the proposed scheme quantitatively attains improved results compared to DBIM.

Next, the proposed scheme is tested for the Latin letters dataset, and the reconstruction results for some representative examples are shown in Figure 7. The DBIM algorithm saturates before 10^{th} iteration, hence the result of proposed method is compared with the DBIM at 10^{th} iteration. The shape

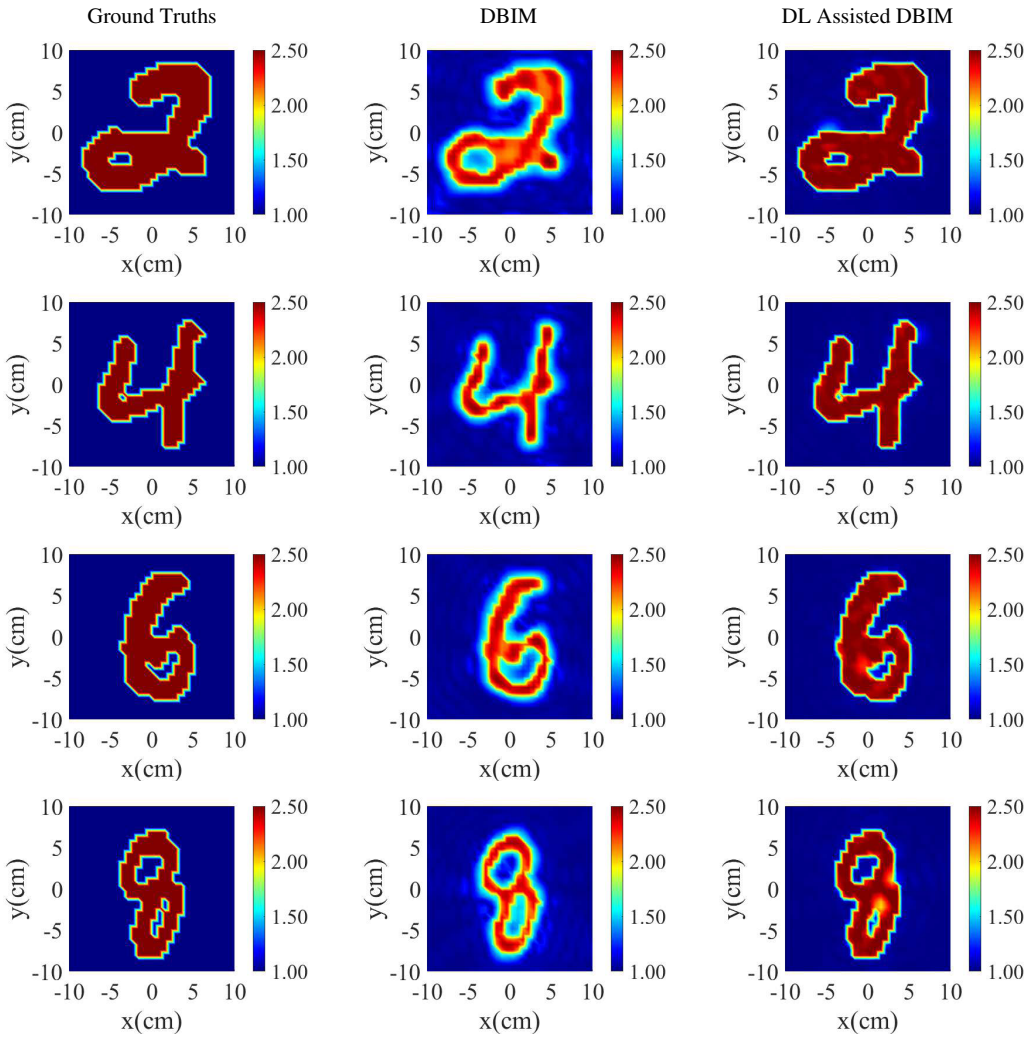

Figure 6. Test results of MNIST digits. The first column is ground truths. The second column is reconstruction by DBIM at the 10^{th} iteration. The third column is a reconstruction by the proposed scheme.

of reconstruction from DBIM at the 10^{th} iteration is good, but the accuracy is less than the proposed method. The respective SSIM and MSE of reconstruction are listed in Table 1.

The proposed scheme is tested for a homogeneous Austria profile with $\epsilon_r = 2.5$. Two smaller discs with a centre ring constitute the Austria profile. The radius of two discs is 0.02 m. A ring's inner and outer radii are 0.05 and 0.07 metres, respectively. Smaller discs are positioned at $(0.035, 0.07)$ m, $(-0.035, 0.07)$ m, and the ring is centred at $(0, -0.02)$ m. Figure 8 presents the reconstructed relative permittivity profiles. The SSIM and MSE for the proposed scheme are 0.9944 and 0.0004, respectively, while for DBIM they are 0.1548 and 0.3476.

To illustrate the improvement of results over each stage, a homogeneous Austria profile having permittivity value 2.5, as shown in Figure 8, is considered. The reconstructed results at each stage of the proposed method are as shown in Figure 9. The SSIM and MSE at each stage are as shown in Table 2. The CNN2 is trained using more data; hence the result is improved over CNN1. There is not much variation in SSIM between CNN2 and the proposed method, but MSE is reduced; also reconstruction of permittivity values is improved, which can be noticed visually in Figure 9(c). Hence, it can be concluded that instead of a single CNN, using cascaded CNN with iterative refinement will provide better results.

The objects' permittivity is chosen between 1.2 and 2.5 for training purposes. It is important

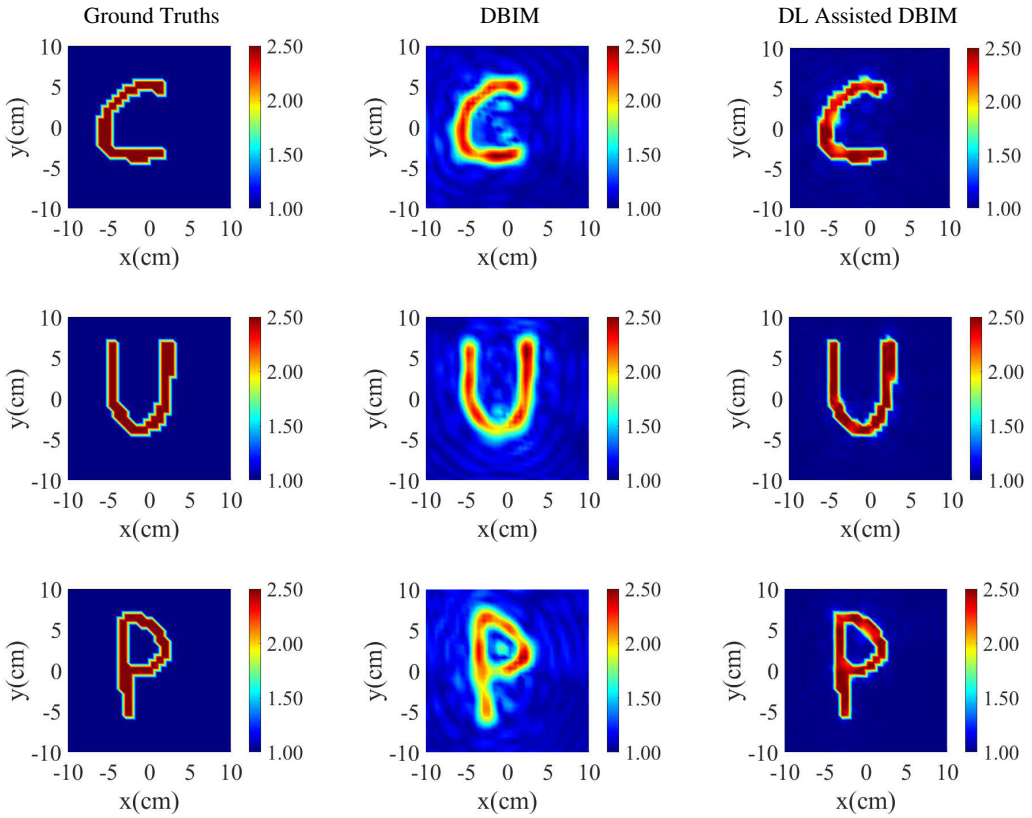

Figure 7. Test results of letters. The first column is ground truths. The second column is reconstruction by DBIM at the 10^{th} iteration. The third column is a reconstruction by the proposed scheme.

Table 1. SSIM and MSE for the tests.

Reference profiles		SSIM		MSE	
		DBIM after 10^{th} iteration	Proposed scheme	DBIM after 10^{th} iteration	Proposed scheme
Digits	2	0.6088	0.9664	0.0561	0.0030
	4	0.7236	0.9784	0.0412	0.0017
	6	0.7246	0.9742	0.0426	0.0026
	8	0.7494	0.9677	0.0370	0.0041
Letters	C	0.5342	0.9106	0.0380	0.0116
	U	0.5224	0.9642	0.0462	0.0062
	P	0.4336	0.9649	0.0629	0.0059
Homogeneous Austria Profile	Profile 1	0.1548	0.9944	0.3476	0.0004
Heterogeneous Austria Profile	Profile 1	0.1456	0.9733	0.3709	0.0033
	Profile 2	0.1455	0.8689	0.3513	0.0158
	Profile 3	0.2326	0.9471	0.2687	0.0068
Heterogeneous Layered Profile	Profile 1	0.0961	0.8174	0.3197	0.0103

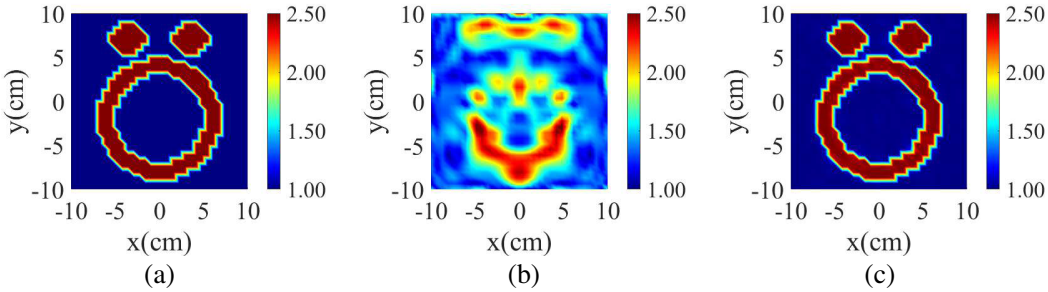

Figure 8. Test results of Austria profile, (a) ground truth, (b) reconstruction by DBIM at 10^{th} iteration, (c) reconstruction by the proposed scheme.

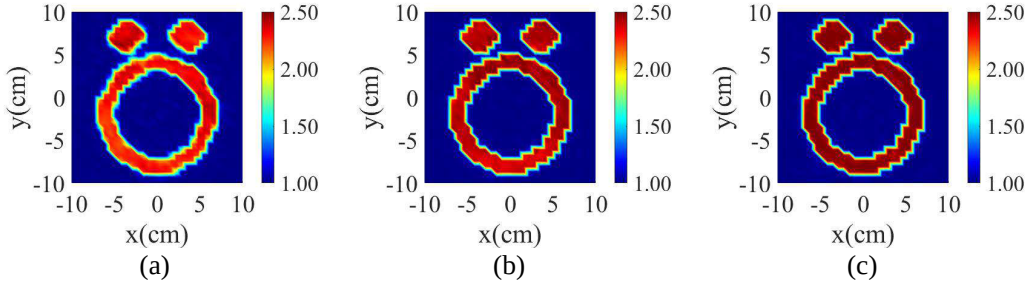

Figure 9. Result of Austria profile at each stage, (a) CNN1, (b) CNN1-CNN2, (c) CNN1-CNN2-DBIM-5 iteration (proposed method).

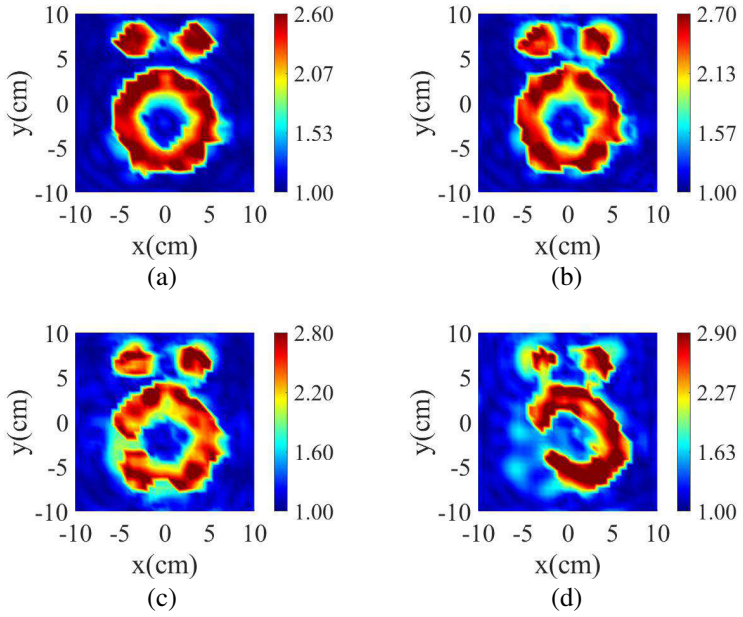

Figure 10. Higher permittivity reconstruction for permittivity, (a) 2.6, (b) 2.7, (c) 2.8 and (d) 2.9.

to note that the proposed CNN scheme also works for a higher range of permittivities if it is trained accordingly. The strength of a scatterer is approximately defined as the product of the contrast and the scatterers approximate size [30]. To reconstruct objects with greater contrast, CNN must be trained using objects of larger electrical dimension [11]. In this work, the proposed trained network is able to give good results up to the relative permittivity 3, and an example is shown in Figure 10. The SSIM

Table 2. SSIM and MSE at each stage for the homogeneous Austria profile in Figure 9.

	SSIM	MSE
CNN1	0.9407	0.0119
CNN1_CNN2	0.9931	0.0012
Proposed method	0.9945	0.0004

Table 3. SSIM and MSE for higher permittivity value.

Permittivity	SSIM	MSE
2.6	0.7065	0.0372
2.7	0.6340	0.0516
2.8	0.5634	0.0717
2.9	0.4155	0.1499

and MSE for various permittivity values are as shown in Table 3. If the neural networks are trained for higher permittivity values, better reconstruction results may be expected, and we will consider this in future works.

4.2. Tests with Heterogeneous Scatterers

The proposed scheme is further tested for heterogeneous Austria profiles, and the results are shown in Figure 11. Profile 1 consists of permittivity 2.5 (ring) and 2.3 (discs). Profile 2 consists of permittivity 2.5, 2.0, and 2.3. Profile 3 consists of permittivity 2.25, 2.0, and 2.5. From the results, it can be concluded that the proposed method is also applicable to effectively reconstruct the heterogeneous scatterers.

In order to further validate the versatility of the proposed method, it is tested for heterogeneously layered profile consisting of concentric cylinders. It consists of an inner cylinder of radius 0.0225 m with $\epsilon_r = 2.5$ and an outer cylinder of radius 0.0225 m with $\epsilon_r = 2.0$. The reconstruction results are displayed in Figure 12. SSIM and MSE for the proposed scheme are 0.8174 and 0.103 respectively while 0.0961 and 0.3197 for DBIM. In this layered profile, permittivity is abruptly changed from 2.0 to 2.5. Hence, the applicability of deep learning does not limited to smoothly varying permittivities.

4.3. Testing with Experimental Data

The proposed scheme is also tested on experimental data provided by Fresnel Institute [17]. Specifically, the "FoamDielExt" profile consisting of two heterogeneous cylinders as shown in Figure 12(a) is considered. The experimental setup consists of an anechoic chamber with 241 receivers (placed from 60° to 300° at a spacing of 1°) and 8 transmitters (placed from 0° to 315° at a spacing of 45°) placed at a distance of 1.67 m from the center of the object. The permittivities of larger cylinder and smaller cylinder are 3 ± 0.3 and 1.45 ± 0.15, respectively. Although the training configuration is significantly different from the experimental configuration, the reconstruction results are satisfactory as shown in Figure 13.

4.4. Comparison of Results

Quantitatively the proposed method is compared with two recent novel methods, Back Propagation-Direct Sampling Approach (BP-DSM) [34] and Subspace-Based Variational Born Iterative Method based Deep Learning method (SVBIM-DL) [12] for Austria profile. Table 4 compares the suggested method's Root Mean Square Error (RMSE) values to those of the BP-DSM and SVBIM-DL approaches. The error values show that the proposed method is more accurate than the other two ways.

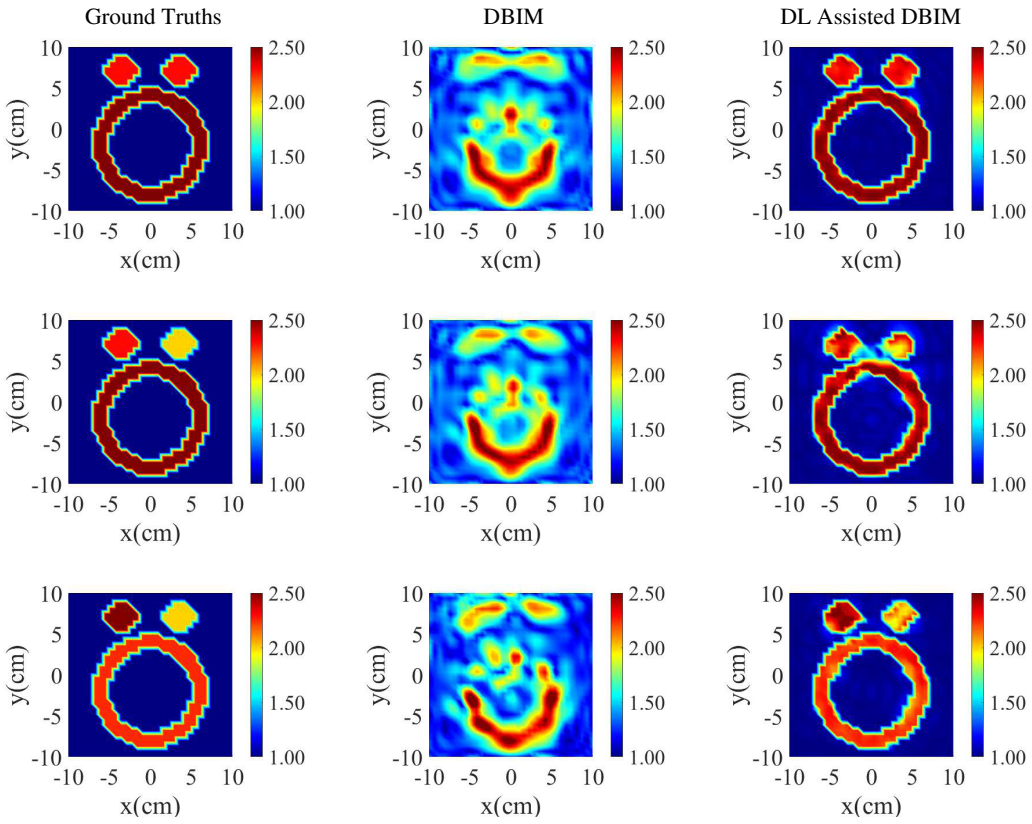

Figure 11. Test results of heterogeneous Austria profile. The first column is ground truth. The second column is a reconstruction by DBIM at the 10^{th} iteration. The third column is a reconstruction by the proposed scheme.

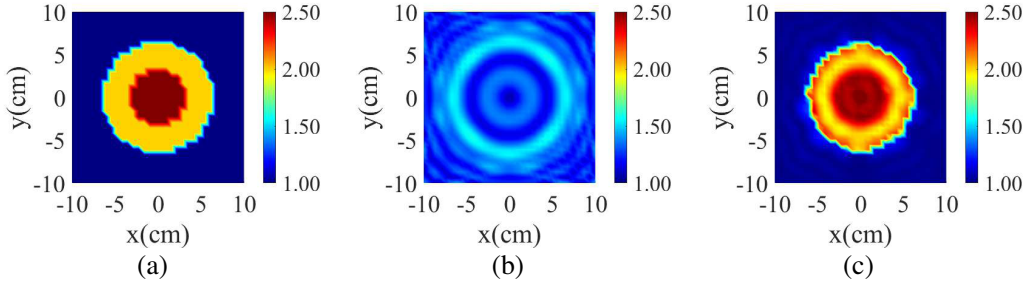

Figure 12. Test results of heterogeneous layered profile, (a) ground truth, (b) reconstruction by DBIM at 10^{th} iteration, (c) reconstruction by the proposed scheme.

Table 4. Reconstruction errors for Austria profile with different schemes.

	Reconstructed Error (RMSE)
BP-DSM [31]	0.1070
SVBIM-DL [12]	0.0813
Proposed	0.0671

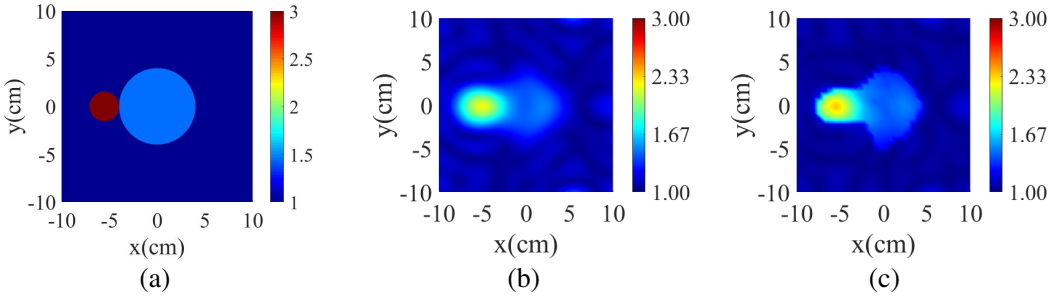

Figure 13. Test results of Fresnel 2005 experimental data "FoamDielExt". (a) Original profile. The larger cylinder has a diameter of 80 mm with relative permittivity of 1.45 ± 0.15. The smaller cylinder has a diameter of 31 mm with relative permittivity of 3 ± 0.3. (b) Reconstruction by DBIM at 10^{th} iteration. (c) Reconstruction by the proposed scheme.

4.5. Noise Analysis

The reconstruction from noisy data is used to demonstrate the stability of the proposed model. The scattered field of the homogeneous Austria profile shown in Figure 8 is contaminated by a random noise SNR = 5 dB, 15 dB, 25 dB, 35 dB, 45 dB, and 55 dB. The SSIM and MSE of proposed scheme and the DBIM reconstruction at the 10^{th} iteration for a various signal-to-noise ratio are shown in Table 5. It can be seen that the use of CNN with DBIM improves the reconstruction significantly over conventional algorithm even for the input data corrupted by noise. The limitation of the proposed method with respect to sensitivity to noise of ISP is that when the SNR is below 10 dB, the reconstruction quality is relatively reduced (Section 4).

Table 5. SSIM and MSE for noise contaminated homogeneous Austria profile.

Noise level		5 dB	15 dB	25 dB	35 dB	45 dB	55 dB
SSIM	DBIM 10^{th} iteration	0.1121	0.1522	0.1631	0.1651	0.1656	0.1657
	Proposed scheme	0.4770	0.8109	0.9631	0.9938	0.9951	0.9954
MSE	DBIM 10^{th} iteration	0.3039	0.2822	0.2804	0.2802	0.2802	0.2802
	Proposed scheme	0.0886	0.0116	0.0022	0.0005	0.0004	0.0004

For SNR = 25 dB to 55 dB, there is not much variation in MSE in the proposed scheme indicating improved stability.

5. CONCLUSION

In this paper, a DBIM-based deep learning approach is introduced to obtain an approximate solution to the ISP in microwave imaging. In this work, cascaded CNN is used where an initial guess by the DBIM is fed to CNN1, and the obtained image is further improved by cascading CNN2. This improved initial guess is given to an iterative algorithm to get the final results. It is worth mentioning that the performance of DBIM with deep learning has not been stated before. Here, a U-Net CNN architecture is implemented that learns the governing equations of the electromagnetic inverse scattering system. The network is trained by generating the reference profiles of MNIST digits, Latin letters, Austria profiles, and different overlapping objects. Thereafter, this trained model is tested on various examples including synthetic and experimental datasets. Results indicate the network's ability to remove artifacts (noise) that were present with the conventional reconstruction algorithms. It is also found that the proposed scheme outperforms conventional DBIM in terms of error. A more advanced architecture can yield even better results, which will be explored in our subsequent studies.

ACKNOWLEDGMENT

The research work carried out in this paper is supported by the Core Research Grant, SERB, India, File No. CRG/2020/004127.

REFERENCES

1. Pastorino, M., *Microwave Imaging*, John Wiley & Sons, 2010.
2. Nikolova, N. K., *Introduction to Microwave Imaging*, Cambridge University Press, 2017.
3. Van Den Berg, P. M. and R. E. Kleinman, "A contrast source inversion method," *Inverse Problems*, Vol. 13, No. 6, 1607, 1997.
4. Chew, W. C. and Y.-M. Wang, "Reconstruction of two-dimensional permittivity distribution using the distorted born iterative method," *IEEE Transactions on Medical Imaging*, Vol. 9, No. 2, 218–225, 1990.
5. Chen, X., "Subspace-based optimization method for solving inverse-scattering problems," *IEEE Transactions on Geoscience and Remote Sensing*, Vol. 48, No. 1, 42–49, 2009.
6. Jin, K. H., M. T. McCann, E. Froustey, and M. Unser, "Deep convolutional neural network for inverse problems in imaging," *IEEE Transactions on Image Processing*, Vol. 26, No. 9, 4509–4522, 2017.
7. Sun, Y., Z. Xia, and U. S. Kamilov, "Efficient and accurate inversion of multiple scattering with deep learning," *Optics Express*, Vol. 26, No. 11, 14678–14688, 2018.
8. Wei, Z. and X. Chen, "Deep-learning schemes for full-wave nonlinear inverse scattering problems," *IEEE Transactions on Geoscience and Remote Sensing*, Vol. 57, No. 4, 1849–1860, 2018.
9. Li, L., L. G. Wang, F. L. Teixeira, C. Liu, A. Nehorai, and T. J. Cui, "DeepNIS: Deep neural network for nonlinear electromagnetic inverse scattering," *IEEE Transactions on Antennas and Propagation*, Vol. 67, No. 3, 1818–1825, 2018.
10. Yao, H. M., E. Wei, and L. Jiang, "Two-step enhanced deep learning approach for electromagnetic inverse scattering problems," *IEEE Antennas and Wireless Propagation Letters*, Vol. 18, No. 9, 2254–2258, 2019.
11. Sanghvi, Y., Y. Kalepu, and U. K. Khankhoje, "Embedding deep learning in inverse scattering problems," *IEEE Transactions on Computational Imaging*, Vol. 6, 46–56, 2019.
12. Anjit, T., R. Benny, P. Cherian, and P. Mythili, "Non-iterative microwave imaging solutions for inverse problems using deep learning," *Progress In Electromagnetics Research M*, Vol. 102, 53–63, 2021.
13. Yin, W., J. Ge, P. Meng, and F. Qu, "A neural network method for the inverse scattering problem of impenetrable cavities," *Electronic Research Archive*, Vol. 28, No. 2, 1123–1142, 2020.
14. Meng, P., X. Wang, and W. Yin, "A dynamical system view on recurrent neural networks," *Electronic Research Archive*, Vol. 30, No. 1, 257–271, 2022.
15. Chen, B., Y. Guo, F. Ma, and Y. Sun, "Numerical schemes to reconstruct three-dimensional time-dependent point sources of acoustic waves," *Inverse Problems*, Vol. 36, No. 7, 075009, 1–21, 2020.
16. Ronneberger, O., P. Fischer, and T. Brox, "U-net: Convolutional networks for biomedical image segmentation," *International Conference on Medical Image Computing and Computer-assisted Intervention*, 234–241, Springer, 2015.
17. Geffrin, J.-M., P. Sabouroux, and C. Eyraud, "Free space experimental scattering database continuation: Experimental set-up and measurement precision," *inverse Problems*, Vol. 21, No. 6, S117, 2005.
18. Franchois, A. and C. Pichot, "Microwave imaging-complex permittivity reconstruction with a Levenberg-Marquardt method," *IEEE Transactions on Antennas and Propagation*, Vol. 45, No. 2, 203–215, 1997.
19. Peterson, M. R. and S. L. Ray, *Computational Methods for Electromagnetics*, Wiley-IEEE Press, New York, 1998.

20. Wang, W. and S. Zhang, "Unrelated illumination method for electromagnetic inverse scattering of inhomogeneous lossy dielectric bodies," *IEEE Transactions on Antennas and Propagation*, Vol. 40, No. 11, 1292–1296, 1992.
21. Li, D., "The MNIST database of handwritten digit images for machine learning research," *IEEE Signal Processing Magazine*, Vol. 29, No. 6, 141–142, 2012.
22. Magdum, A., M. Erramshetty, and R. P. K. Jagannath, "An exponential filtering based inversion method for microwave imaging," *Radioengineering*, Vol. 30, No. 3, 496–503, 2021.
23. Wang, Z., A. C. Bovik, H. R. Sheikh, and E. P. Simoncelli, "Image quality assessment: From error visibility to structural similarity," *IEEE Transactions on Image Processing*, Vol. 13, No. 4, 600–612, 2004.
24. Vargas, J. O., A. C. Batista, L. S. Batista, and R. Adriano, "On the computational complexity of the conjugate-gradient method for solving inverse scattering problems," *Journal of Electromagnetic Waves and Applications*, Vol. 35, No. 17, 2323–2334, 2021.
25. Khoshdel, V., A. Ashraf, and J. LoVetri, "Enhancement of multimodal microwave-ultrasound breast imaging using a deep-learning technique," *Sensors*, Vol. 19, No. 18, 4050, 2019.
26. Wei, Z., D. Liu, and X. Chen, "Dominant-current deep learning scheme for electrical impedance tomography," *IEEE Transactions on Biomedical Engineering*, Vol. 66, No. 9, 2546–2555, 2019.
27. Wei, Z. and X. Chen, "Physics-inspired convolutional neural network for solving full-wave inverse scattering problems," *IEEE Transactions on Antennas and Propagation*, Vol. 67, No. 9, 6138–6148, 2019.
28. Kandel, I. and M. Castelli, "The effect of batch size on the generalizability of the convolutional neural networks on a histopathology dataset," *ICT Express*, Vol. 6, No. 4, 312–315, 2020.
29. Ye, X., Y. Bai, R. Song, K. Xu, and J. An, "An inhomogeneous background imaging method based on generative adversarial network," *IEEE Transactions on Microwave Theory and Techniques*, Vol. 68, No. 11, 4684–4693, 2020.
30. Habashy, T. M., R. W. Groom, and B. R. Spies, "Beyond the born and Rytov approximations: A nonlinear approach to electromagnetic scattering," *Journal of Geophysical Research: Solid Earth*, Vol. 98, No. B2, 1759–1775, 1993.
31. Chen, X., *Computational Methods for Electromagnetic Inverse Scattering*, John Wiley & Sons, 2019.
32. Chew, W. C. and Q.-H. Liu, "Inversion of induction tool measurements using the distorted Born iterative method and CG-FFHT," *IEEE Transactions on Geoscience and Remote Sensing*, Vol. 32, No. 4, 878–884, 1994.
33. He, K. and J. Sun, "Convolutional neural networks at constrained time cost," *IEEE Conference on Computer Vision and Pattern Recognition*, 5353–5360, 2015.
34. Zhang, L., K. Xu, R. Song, X. Ye, G. Wang, and X. Chen, "Learning-based quantitative microwave imaging with a hybrid input scheme," *Electronic Research Archive*, Vol. 28, No. 24, 15007–15013, 2020.